ACS Infectious Diseases

pubs.acs.org/journal/aidcbc

Article

α2,6-Sialylation Is Upregulated in Severe COVID-19, Implicating the Complement Cascade

Published as part of the ACS Infectious Diseases virtual special issue "Glycoscience in Infectious Diseases".

Rui Qin,◆ Emma Kurz,◆ Shuhui Chen,◆ Briana Zeck, Luis Chiribogas, Dana Jackson, Alex Herchen, Tyson Attia, Michael Carlock, Amy Rapkiewicz, Dafna Bar-Sagi, Bruce Ritchie, Ted M. Ross, and Lara K. Mahal*

Cite This: https://doi.org/10.1021/acsinfecdis.2c00421

Read Online

ACCESS | Metrics & More | Article Recommendations | Supporting Information

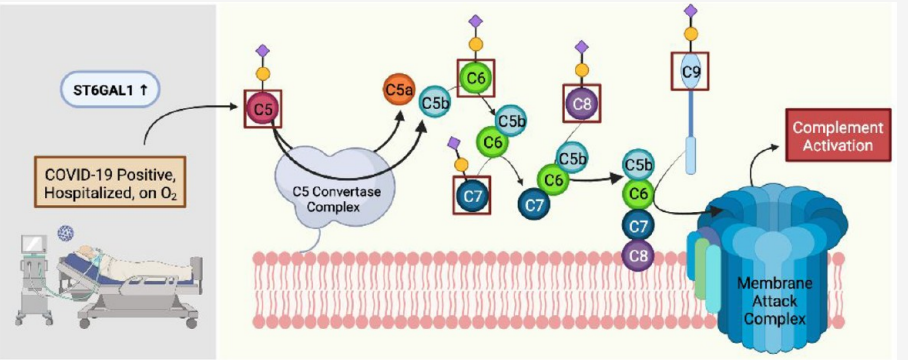

ABSTRACT: Better understanding of the molecular mechanisms underlying COVID-19 severity is desperately needed in current times. Although hyper-inflammation drives severe COVID-19, precise mechanisms triggering this cascade and what role glycosylation might play therein are unknown. Here we report the first high-throughput glycomic analysis of COVID-19 plasma samples and autopsy tissues. We find that α2,6-sialylation is upregulated in the plasma of patients with severe COVID-19 and in autopsied lung tissue. This glycan motif is enriched on members of the complement cascade (e.g., C5, C9), which show higher levels of sialylation in severe COVID-19. In the lung tissue, we observe increased complement deposition, associated with elevated α2,6-sialylation levels, corresponding to elevated markers of poor prognosis (IL-6) and fibrotic response. We also observe upregulation of the α2,6-sialylation enzyme ST6GAL1 in patients who succumbed to COVID-19. Our work identifies a heretofore undescribed relationship between sialylation and complement in severe COVID-19, potentially informing future therapeutic development.

KEYWORDS: *glycosylation, sialic acid, lectin microarray, SARS-CoV-2, complement, lectin array*

COVID-19, the clinical syndrome caused by SARS-CoV-2 infection, varies in severity from mild respiratory symptoms to pneumonia requiring hospitalization to death.[1] Over the last two years, the immune response in COVID-19 has been studied in an effort to characterize disease pathology and better understand the potential therapeutic options for severe COVID-19. One of the milestones of severe COVID-19 is hyper-inflammation, which is associated with acute respiratory distress syndrome (ARDS), dysregulation of cytokine release, NFκB signaling and immune cell mobilization, thrombosis, increased vascular permeability, and endothelial damage.[2,3] The complement cascade is an important trigger of inflammation and has been shown to be activated in COVID-19 in multiple studies.[4] This proteolytic cascade produces various pro-inflammatory molecules and results in the formation of the membrane attack complex (MAC) that causes cell death and tissue damage. In severe COVID-19, the augmented inflammatory signatures, including formation of neutrophil extracellular traps (NETs), increased myeloid cell recruitment, and higher cytokine levels, all map onto dysregulation of the complement cascade.[5] Therefore, there has been an increasing interest in evaluating the therapeutics for severe COVID-19 that specifically target the complement cascade.[6]

Received: August 14, 2022

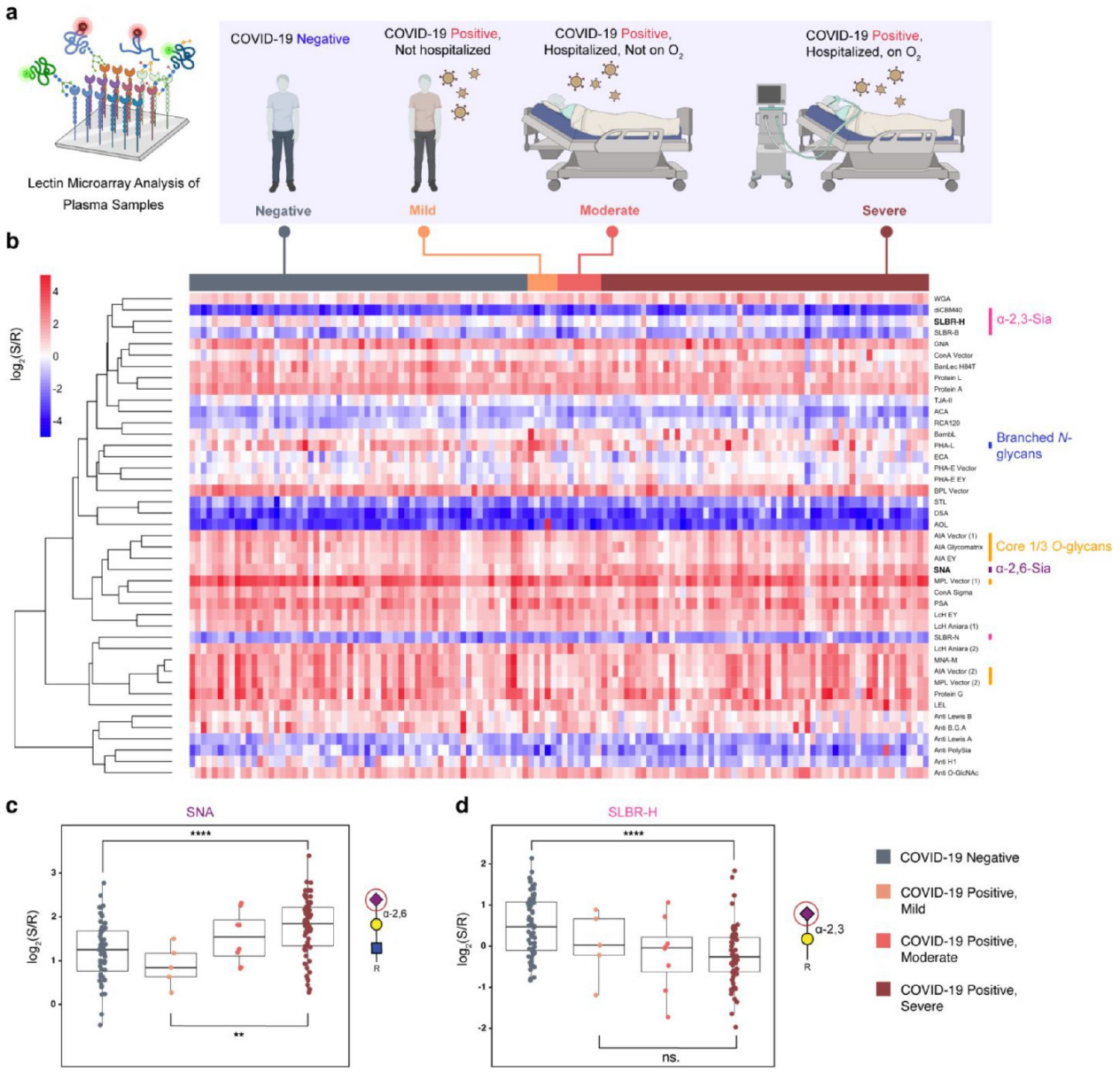

Figure 1. Plasma glycomic profiles of COVID-19-positive and -negative cohorts. (a) Schematic description of analysis. COVID-19-positive patients were categorized into three groups by disease severity (Mild, Moderate, and Severe) and compared to an age and gender-matched control cohort (Negative). Plasma samples were analyzed by lectin microarray. (b) Heatmap of lectin microarray data with annotations of rough glycan specificities for select lectins. Columns (patients) are ordered by disease severity as in (a), indicated at the top of the heatmap. (c) Box plot analysis of SNA and SLBR-H binding data by patient group. All statistically significant differences are indicated. Glycan ligands for the lectins are shown in the Symbolic Nomenclature for Glycomics (SNFG). Symbols are defined as follows: galactose (yellow, ●), *N*-acetylglucosamine (blue, ■), sialic acid (purple, ♦). Mann−Whitney U test was used to determine *p* values: ns, not statistical; $*p < 0.05$; $**p < 0.01$; $***p < 0.001$; $****p < 0.0001$.

Glycosylation plays essential and increasingly appreciated roles in regulating inflammation and immune response in infectious diseases.[7−9] Antibody-mediated responses are impacted by glycosylation. In IgG, core fucosylation inhibits interactions with Fc receptors, diminishing antibody-dependent cellular cytotoxicity (ADCC).[8] Several other glycan features, including sialylation, bisecting GlcNAc, and galactosylation, have also been associated with IgG function.[8] Glycosylation also plays a key role in the host immune response to pathogens, which determines the disease severity.[7] In recent work on influenza, severe disease correlated with a high expression of high mannose in the lung, a glycoform that binds the innate immune receptor mannose binding lectin (MBL2).[10] In COVID-19, glycosylation patterns of SARS-CoV-2-specific antibodies correlated with severity. Lower core fucosylation was associated with higher severity, in line with the impact of this modification on ADCC.[11,12] Although IgG glycosylation was studied in COVID-19, to date there has been no work examining the relationship between glycosylation and severity in whole plasma or glycomic changes in affected tissues.

In this work, we utilized our high-throughput lectin microarray technology[13,14] to examine glycosylation as a function of COVID-19 severity in both plasma and autopsy tissues, with a focus on identifying glycomic markers of severity and understanding their potential roles. We found higher levels of α2,6-sialylation in the plasma of severe COVID-19 patients, which was also observed in the lower lobes of the lungs in

https://doi.org/10.1021/acsinfecdis.2c00421
ACS Infect. Dis. XXXX, XXX, XXX−XXX

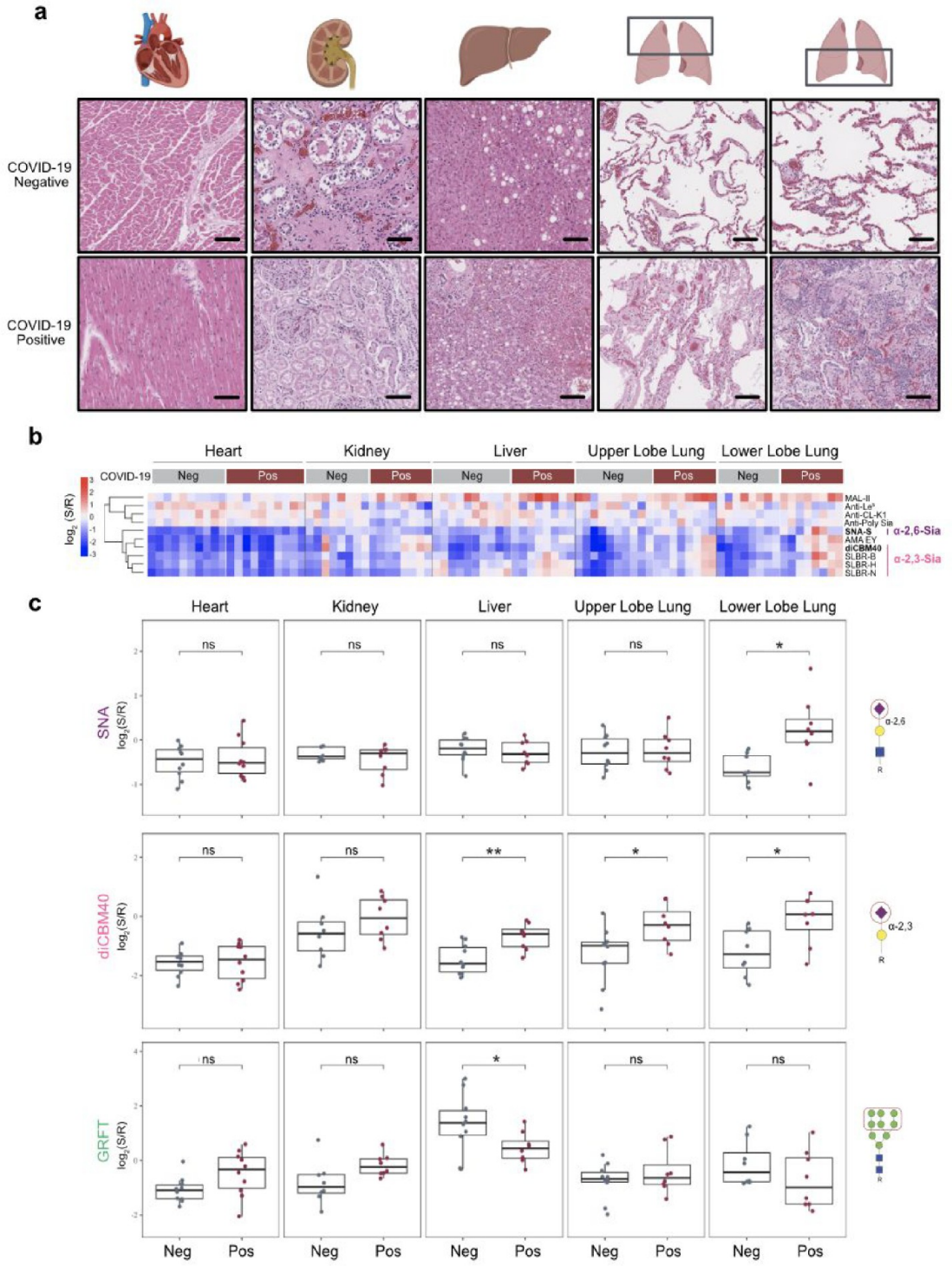

Figure 2. Organ-specific glycan changes are observed in COVID-19 patients. (a) Representative images of H&E stains of organs from COVID-19-positive and COVID-negative autopsy samples (heart, $n = 5$; kidney, $n = 4$; liver, $n = 4$; upper lobe lung, $n = 4$; lower lobe lung, $n = 4$; 2 samples per patient). Scale bars represent 75 μm. (b) Heatmap presenting statistically significant lectins ($p < 0.05$, Student's t test) from lectin microarray analysis. Samples from COVID-positive (heart, $n = 5$; kidney, $n = 4$; liver, $n = 4$; upper lobe lung, $n = 4$; lower lobe lung, $n = 4$; 2 samples per patient) and COVID-negative (heart, $n = 5$; kidney, $n = 4$; liver, $n = 5$; upper lobe lung, $n = 5$; lower lobe lung, $n = 4$; 2 samples per patient) patients were analyzed. Lectins were hierarchically clustered using Pearson correlation coefficient and average linkage analysis. Median normalized $\log_2$ ratios (sample (S)/reference (R)) were ordered by sample type. Red, $\log_2(S) > \log_2(R)$; blue, $\log_2(R) > \log_2(S)$. (c) Box plot analysis of α-2,6-sialic acids probed by SNA. Box plot analysis of α-2,3-sialic acids probed by diCBM40. Box plot analysis of high mannose probed by GRFT. Data is from analysis shown in (a). COVID-19-positive (maroon), COVID-negative controls (gray). Student's t test was used to determine p-values. ns, not statistical; *$p < 0.05$; **$p < 0.01$; ***$p < 0.001$; ****$p < 0.0001$. Glycans bound by lectins are shown at the right side of the box plots.

patients who succumbed to COVID-19. In the severe cases, plasma glycoproteins bearing this epitope were enriched in members of the complement cascade, which had a greater fraction of α2,6-sialylated protein compared to the mild cases.

https://doi.org/10.1021/acsinfecdis.2c00421
ACS Infect. Dis. XXXX, XXX, XXX−XXX

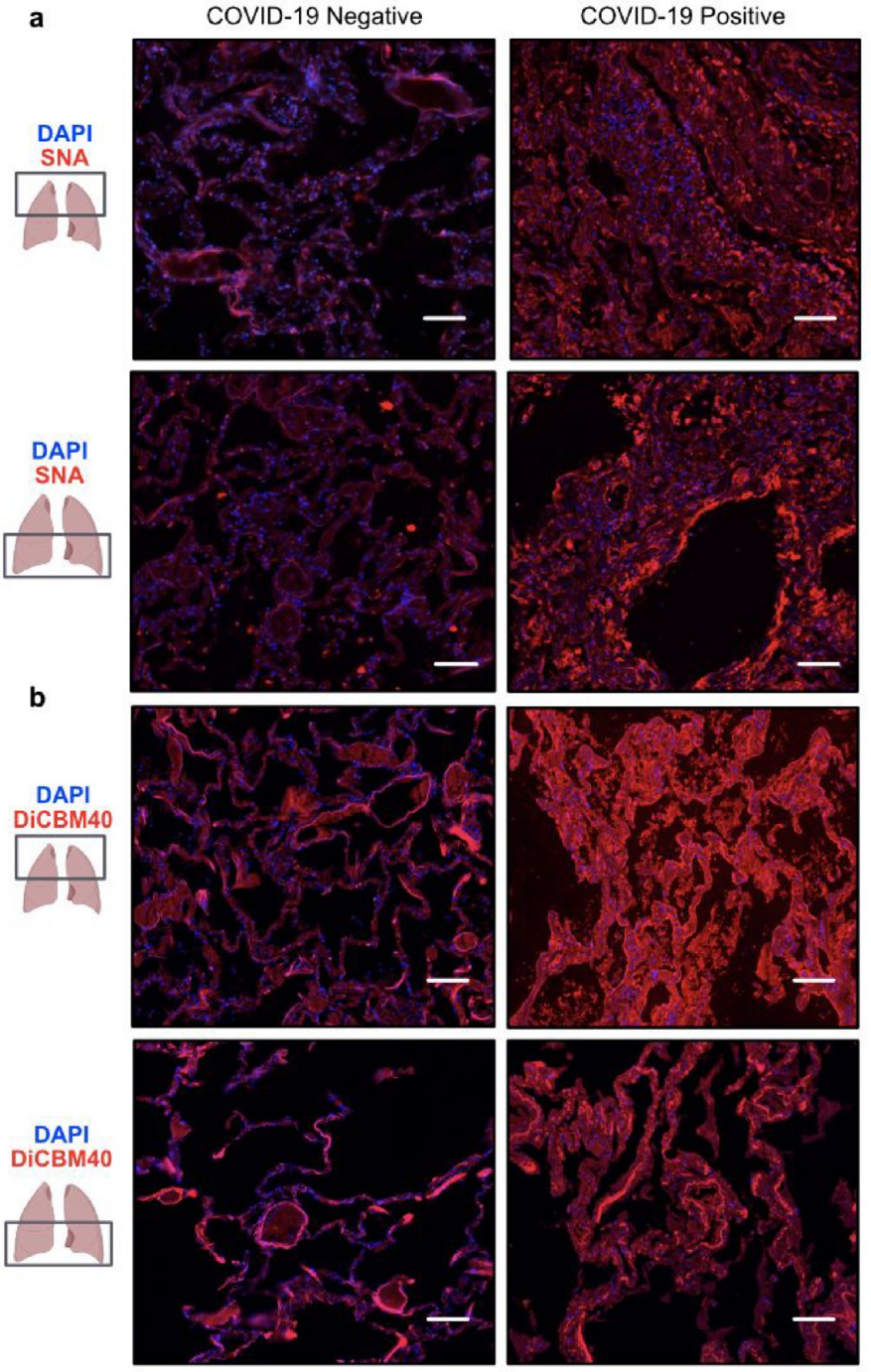

Figure 3. Expression of α2,6-sialic acid (SNA) and α2,3-sialic acid (diCMB40) in upper and lower lobes of COVID-19 autopsy lungs. (a) Representative images of immunofluorescence (IF) staining against SNA in the upper lobe (top) or lower lobe (bottom) of the lungs of COVID-19-negative (n = 2) or COVID-19-positive (n = 8) autopsy specimens. Scale bars represent 150 μm. (b) Representative images of IF staining against diCBM40 in the upper lobe (top) or lower lobe (bottom) of the lungs of COVID-19-negative (n = 2) or COVID-19-positive (n = 8) autopsy specimens. Scale bars represent 150 μm.

Complement deposition and increased myeloid recruitment were observed in the lower lobe lungs of COVID-19 autopsies. We also identified higher levels of ST6GAL1, the main enzyme that biosynthesizes α2,6-sialic acid, in COVID-19 patients. Overall, our work points to a previously unexplored role of α2,6-sialylation in complement system biology. This newly discovered association may have important consequences for the development of therapeutic approaches to ameliorate the detrimental immune responses resulting from the overactivated complement cascade in severe COVID-19.

RESULTS

α2,6-Sialylation Is Upregulated in the Plasma of Severe COVID-19 Patients. COVID-19 severity is highly variable, ranging from asymptomatic disease to acute respiratory distress syndrome (ARDS) and death.[1] While glycosylation of SARS-CoV-2-specific IgG has been identified

https://doi.org/10.1021/acsinfecdis.2c00421
ACS Infect. Dis. XXXX, XXX, XXX−XXX

as a severity marker,[11,12] there have been no broader analyses of glycosylation in plasma with regards to COVID-19. Herein, we examined the glycosylation of plasma from a cohort of 71 SARS-CoV-2-positive adults recruited at the University of Alberta Hospital. The majority of samples were collected during the second wave of COVID-19 from October 2020 to January 2021 (Supporting Information, Table S1). During this time, variants had not yet emerged and the original Sars-CoV-2 strain was dominant.[15] Plasma samples were collected at the first hospital visit or at the time of a SARS-CoV-2-positive PCR test. We categorized the COVID-19-positive patients into three severity groups: (i) patients who were not hospitalized (mild, $n = 5$), (ii) patients who were hospitalized but did not need supplemental oxygen (moderate, $n = 8$), and (iii) patients who were hospitalized, received supplemental oxygen, and/or were in the ICU (severe, $n = 58$). As a negative control, we used prepandemic plasma samples from an age- and gender-matched healthy cohort ($n = 60$) recruited at the University of Georgia (Figure 1a).

To analyze the glycome, we performed our dual-color lectin microarray analysis on the plasma samples (left panel, Figure 1a). Lectin microarray technology utilizes a collection of specific, well-characterized glycan-binding proteins[16] to evaluate differential glycan expression patterns between sample groups.[14] An advantage of this method is that probes that identify significant changes in the glycome can then be used for further glycoproteomic and histochemical studies. High-throughput glycomic analysis using our established array technology has revealed new roles for glycans in cancer biology,[17] host−pathogen interactions,[18,19] and vaccine response.[20] In brief, each sample was fluorescently labeled (*S*, Alexa Fluor 555 labeled) and mixed with an equal amount of an orthogonally labeled reference standard (*R*, Alexa Fluor 647 labeled commercial plasma). Samples were analyzed using in-house fabricated lectin microarrays containing >95 probes (Tables S4 and S5), as previously described.[13] A heatmap of the normalized $\log_2$ data (S/R) from our COVID-19 positive and control plasma samples is shown in Figure 1b.

Comparison of all COVID-19-positive samples to the controls identified several distinct glycomic changes with infection (Figure S1). We observed a significant loss of core 1,3-*O*-glycans (AIA), α2,3-sialic acid (SLBR-H, SLBR-B), and β1,6-branched *N*-glycans (PHA-L) and an increase in α2,6-sialic acid (SNA). Closer examination of differences in glycosylation between the severity groups revealed changes in the levels of total α2,6-sialylation of glycoproteins as a function of severity. Patients with severe COVID-19 had significantly higher levels of α2,6-sialylation when compared to either the negative controls or the mild COVID-19 cohort (severe vs negative, ∼45% increase; severe vs mild, ∼84% increase; Figure 1c). In contrast, although lower levels of α2,3-sialylation were observed, we did not see severity-dependent changes (SLBR-H, SLBR-B, diCBM40; Figures 1d and S2). Overall, we observed both infection- and severity-dependent changes in the plasma glycome in COVID-19.

Post-mortem COVID-19 Patients Exhibited a Significant Increase in Sialylation in Select Tissues. COVID-19 can affect multiple organs, causing thromboembolism, kidney injury, damage to the heart, etc.[1,21] To investigate whether changes in plasma are reflective of changes in tissue from COVID-19 patients, we conducted a glycomic analysis of autopsy tissue samples using our lectin microarrays. Tissues were obtained from patients who either succumbed to COVID-19 during the initial phase of the pandemic in New York City (positive, pos; original SARS-CoV-2 strain) or individuals who died of other causes (negative, neg).[22] The majority of patients in the cohort had lung pathology. More specific patient characteristics are given in Table S2. We confirmed the histological integrity and quality of the autopsy tissues (heart, kidney, liver, and upper and lower lobes of the lung) by the presence of intact nuclei in hematoxylin and eosin (H&E) staining (Figure 2a). A heatmap showing a significant difference in glycomic assessment of autopsy tissues is shown in Figure 2b. A complete heatmap of lectin microarray data organized by tissue type and COVID status is shown in Figure S3.

Tissue-dependent patterns were observed in our analysis, regardless of mode of death. This follows previous work that showed that the glycome could be used to segregate cell lines by cancer tissue origin and indicates that glycosylation is a marker of tissue type.[23] Within tissues, we observed several COVID-dependent glycan signatures (Figure S4). SARS-CoV-2 infections begin in the nasal passages before migrating to the lung, where they cause significant damage that can result in death. It should be noted that the majority of our matched controls exhibited pulmonary pathology upon autopsy (Table S2). In concordance with our plasma data, an increase in α2,6-sialylation was seen in the lower lobe but not the upper lobe of the lung in COVID-19 patients. In many respiratory illnesses, damage to the lower lobe of the lung is associated with more advanced disease.[24] In contrast to our data from plasma, we also observed a significant increase in α2,3-sialic acid in COVID patients. This increase was seen in both the upper and lower lobes of the lung and in liver tissues (diCBM40, Figure 2c; SLBR-B, SLBR-N, and SLBR-H, Figure S5). We also see several other changes in glycosylation in the COVID-positive cohort that are predominantly in the liver. This group has lower levels of high mannose (GRFT and BanLec H84T, Figure 2c) and higher levels of core 1,3-*O*-glycans (MPA, MNA-G; Figure S6). Interestingly, higher, albeit nonstatistical, levels of high mannose are observed in heart and kidney, both of which have been shown in other systems to undergo MBL2-mediated damage.[25,26]

We corroborated our lectin microarray findings using lectin fluorescence staining within the same cohort of autopsy specimens. Overall, the staining confirmed the lectin microarray findings, including an increase in α2,6-sialic acid in the lower lobe of the lungs (SNA, Figure 3a), an increase in α2,3-sialic acid in both lung compartments (diCBM40, Figure 3b) and the liver (diCBM40, Figure S7), and a decrease in high mannose in the livers of COVID-19 patients (GRFT, Figure S7). The upper lobe lung of COVID-19 patients also showed slightly higher α2,6-sialic acid staining (SNA, Figure 3a), although the magnitude of the increase was significantly smaller than that observed in the lower lobes.

Complement Proteins Are Differentially Sialylated in Severe COVID-19. Higher levels of α2,6-sialic acid were observed in both our plasma and autopsy cohorts, leading us to wonder whether there was a mechanistic link between these two findings. With this in mind, we conducted α2,6-sialic acid-focused glycoproteomic analysis using pooled plasma from the same cohort on which we ran glycomic analysis. In brief, we pooled the plasma of the mild COVID-19 patients and the severe COVID-19 patients and performed SNA pulldown on the two pooled plasma samples. SNA-enriched proteins were then identified using standard mass spectrometry (Figure 4a).

https://doi.org/10.1021/acsinfecdis.2c00421
ACS Infect. Dis. XXXX, XXX, XXX−XXX

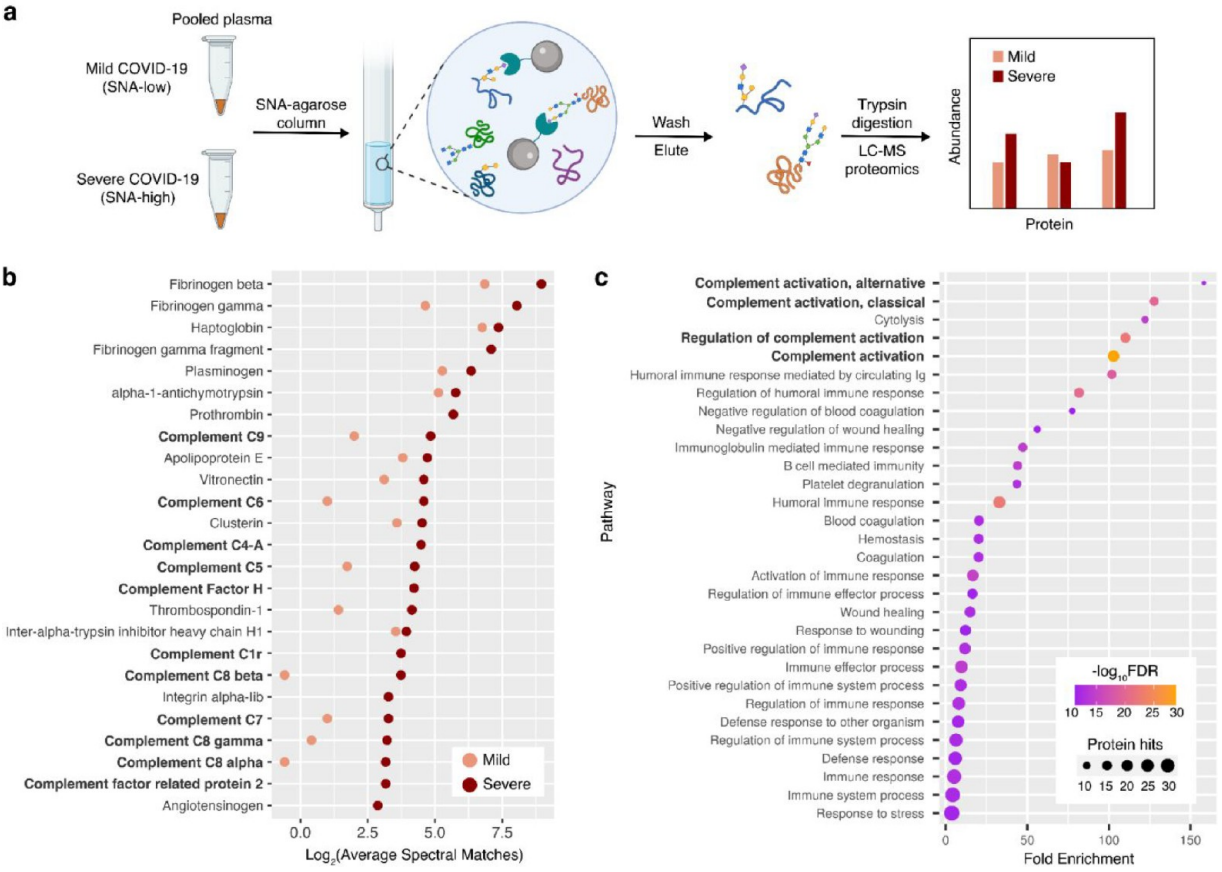

Figure 4. Glycoproteomic analysis of α2,6-sialic acid-containing proteins from mild and severe COVID-19 plasma. (a) Scheme of workflow. Mild COVID-19, COVID-19 patients who were not hospitalized; severe COVID-19, COVID-19 patients who were hospitalized and received supplemental oxygen. (b) SNA-reactive glycoproteins significantly enriched the severe COVID-19 plasma compared to the mild, as well as their mass spectrometric abundance profiles (average spectral matches). The top 25 enriched glycoproteins (by abundance) in the severe group are shown. (c) Pathway enrichment analysis of the enriched plasma glycoproteins. Number of protein hits and $-\log_{10}$FDR for pathways are indicated.

We identified 77 proteins in the severe COVID-19 group (Table S5) and 38 in the mild group (Table S6), with 29 proteins identified in common between both groups. This was in line with our expectation, as severe COVID-19 patients showed greater plasma α2,6-sialylation. A total of 44 SNA-enriched glycoproteins were significantly higher in abundance in the severe COVID-19 group compared to the mild group (Figure 4b; Table S7). As expected, we observed many proteins involved in thrombosis and the coagulation cascade, including fibrinogens, plasminogen, and prothrombin. This is consistent with findings in autopsy and other severe COVID-19 cohorts, where dysregulated thrombosis is observed.[3,22] These proteins are often highly abundant in plasma, and enrichment could be due to increases in the expression of mediators of coagulation.[27] Gene ontology enrichment analysis using the differentially expressed proteins identified complement system-related pathways as the most significantly enriched (Figure 4c). This implies that α2,6-sialic acid upregulation may be connected to severe COVID-19 via a mechanistic link involving the complement system. We observed many of the downstream complement cascade members in our enriched pool (C5, C6, C7, C8, and C9; Figures 4b and 5a).

Activation of the complement system in COVID-19 and its association with severity have been reported by multiple groups.[4,27] Both C5 and C9 have been associated with severe COVID-19 and contribute to MAC-induced cell death and damage (Figure 5a).[4,27,28] To gain insight into whether we are observing a change in sialylation or complement levels, we performed SNA pulldowns from pooled plasma samples from mild and severe COVID-19 patients and controls and performed Western blot analysis for C5 and C9 (Figure 5b). In the COVID-19 patients, both C5 and C9 have higher levels of α2,6-sialylation when compared to control, with some evidence of a severity-dependent increase in sialylation for C5. These data suggest an increased fraction of complement is α2,6-sialylated in COVID-19.

Complement proteins can be produced in the liver, immune cells, endothelia, and epithelia.[29,30] In COVID-19 patients, we observed aberrant expression of ST6 β-galactoside α2,6-sialyltransferase 1 (ST6GAL1), the main enzyme responsible for α2,6-sialylation, in the lung epithelia (Figures 5d and S8). We also found high levels of expression of ST6GAL1 in the liver of both COVID-19-positive and -negative patients, consistent with the known expression patterns for this enzyme (Figure S8).[31] Mining of publicly available RNA-seq data[32] showed an increased ratio of ST6GAL1 to C5 in the whole blood of patients with COVID-19 when compared to those with seasonal coronavirus infection or to uninfected controls (Figure 5c). Neither ST6GAL1 nor C5 alone showed significantly different levels in COVID-19 when compared to control (Figure S9). In aggregate these data suggest that an enhanced fraction of α2,6-sialylated complement proteins,

https://doi.org/10.1021/acsinfecdis.2c00421
ACS Infect. Dis. XXXX, XXX, XXX−XXX

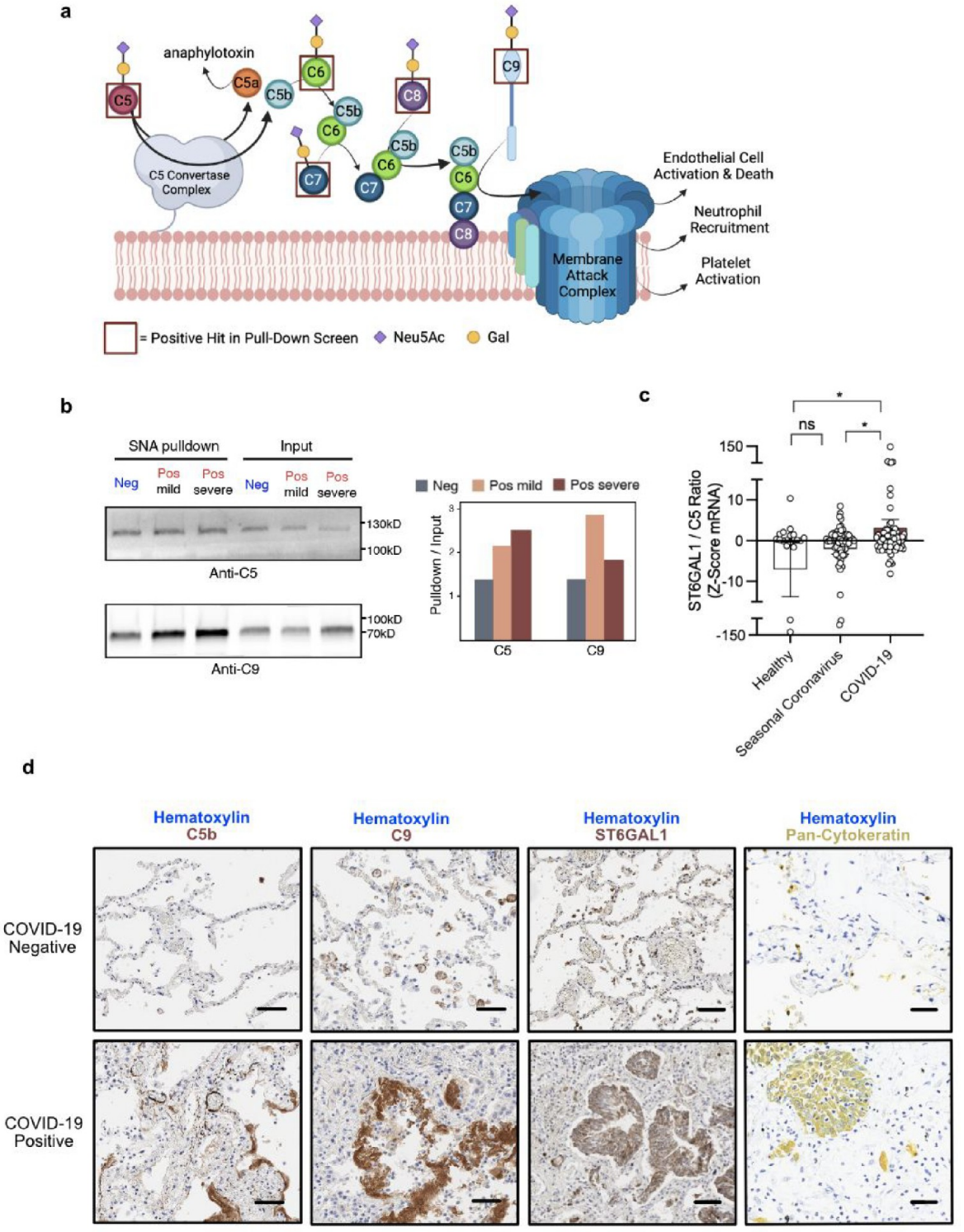

Figure 5. Fraction of α2,6-sialylated complement cascade enriched in COVID-19 blood and lungs. (a) Scheme of the later portion of the complement cascade pathway and downstream signaling. Maroon boxes indicate complement proteins that were positive hits in our glycoproteomic analysis in Figure 4. (b) Differential α2,6-sialylation of complements C5 and C9 in three patient groups. Western blot (anti-C5 and anti-C9) of SNA pulldown samples from pooled patient plasma with corresponding input is shown. Intensity ratios of pulldown/input bands are depicted in the bar plot. (c) Analysis of individual per patient paired ratio of ST6GAL1 to C5 mRNA expression in whole blood of healthy controls (n = 19), those with seasonal coronavirus (n = 59), or those with COVID-19 (n = 46), from publicly available data set Gene Expression Omnibus: GSE161731. Student's t test was used to determine p-values: ns, not statistical; *p < 0.05; **p < 0.01; ***p < 0.001; ****p < 0.0001. (d) Representative images of IHC staining against C5b, C9, ST6GAL1, or Pan-Cytokeratin in the lower lobe of the lungs in COVID-19-negative (n = 2) (top) or COVID-19-positive (n = 8) (bottom) autopsy specimens. Scale bars represent 75 μm.

potentially deriving from multiple compartments, is associated with COVID-19 as a disease state.

To examine whether complement activation is observed in our autopsy cohort, we performed immunohistochemical

https://doi.org/10.1021/acsinfecdis.2c00421
ACS Infect. Dis. XXXX, XXX, XXX−XXX

(IHC) staining for C5b and C9. We observed high levels of C5b and C9 deposition in the livers of COVID-19 patients when compared to controls (Figure S8). We also observed extensive deposition of C5b and C9 in the lungs of COVID-19 patients (Figure 5d). In the lower lobe of the lung, staining for both complement proteins and α2,6-sialic acid is concentrated at the edges of the airway barrier, in line with our observation that complement proteins themselves are sialylated. The complement cascade can have many downstream effects.[4,6] IL-6, which is strongly associated with COVID-19 mortality, is both a promoter of and enhanced by complement activation.[33,34] In line with this, staining of our autopsy cohort showed increased IL-6 levels in the lungs in COVID-19 patients compared to controls (Figure S10). In multiple pathogenic diseases, the complement cascade is profibrotic, acting directly on myeloid cells (e.g., macrophages) and fibroblasts alike.[35,36] The dcomplement is also known to recruit myeloid cells to sites of tissue injury. Recent literature suggests that in COVID-19 there is enhanced pulmonary fibrosis mediated by $CD163^+$ macrophages that exhibit fibroblast-like features.[37] In our cohort, we observed a drastic enrichment of this cell type in the lower lobe of COVID-19-positive lungs (Figure S10). Our cohort showed pathological outcomes characteristic of the complement hyperactivation, suggesting a possible link between sialylation and complement-mediated tissue damage in COVID-19.

DISCUSSION

Glycosylation has multifaceted roles in immunity and host response to pathogens.[7−9] Recognition of glycans helps determine self vs nonself and can trigger immune activation via both the innate and adaptive immune system. In influenza, the severity of disease was found to be associated with levels of high mannose and the innate immune lectin MBL2.[10,18] In SARS-CoV-2 infection, antibody glycosylation has been studied as a marker of severity. Antibodies to the spike protein were altered in severe patients, with lower fucosylation and sialylation observed.[11,12] This has potential consequences for effector function.[8] However, such studies have focused on a single protein type (IgG). To date there has been no work on the systemic glycomic response to SARS-CoV-2 infection in plasma with regards to severity and no analysis of infected tissues.

Herein, we performed high-throughput analysis of plasma and autopsy sample glycosylation from COVID-19 patients using our lectin microarray technology. Our analysis revealed plasma α2,6-sialic acid as a marker of severity. This modification is known to increase the half-life of select proteins, including IgG.[38,39] We also observed higher levels of α2,6-sialic acid in the lower lobe of the lungs in patients who died from COVID-19. In previous studies, CT scans showed that lower lobe involvement and consolidation is common in COVID-19 patients.[40,41] In the lower lobe, staining for α2,6-sialic acid appeared strongest at the barrier of blood-gas exchange.

Glycoproteomic analysis of α2,6-sialylated proteins from plasma showed enrichment in members of the complement cascade. The complement cascade is a proteolytic cascade culminating in the formation of the membrane attack complex (MAC, Figure 5a). Activated through both innate and adaptive immune mechanisms, it stimulates multiple immune responses including myeloid cell mobilization, cytokine release, cell damage, platelet activation, and the coagulation cascade.[35,36] Hyperactivation of the complement cascade is recognized as an emerging therapeutic target for COVID-19.[4,6,27] In line with this, we observed high levels of staining for complement proteins C5 and C9 in COVID-19 autopsy samples. Of note, in the lower lobe lung the staining for complement also localized to the barrier of blood-gas exchange.

In plasma, we found that the fraction of α2,6-sialylated C5 and C9 in severe COVID-19 patients is significantly upregulated (Figure 5b). The increased pool of sialylated complement most likely derived from augmented expression of ST6GAL1, the main enzyme responsible for α2,6-sialylation. We observed upregulation of this enzyme in the lung (Figures 5d and S8). In addition, analysis of previous work found higher relative levels of this enzyme in the blood in COVID-19 patients (Figure 5c). In concordance with our findings, several studies have also shown upregulation of ST6GAL1 in lung epithelium, liver, and immune cells in COVID-19.[42−44] Collectively, the data suggests α2,6-sialylation plays a role in the immune response to COVID-19.

Previous studies have shown that almost all complement proteins can bear sialylated glycans.[45] Factor H, which inhibits the cascade, binds α2,3-sialylation on host cells, a critical aspect of self-recognition.[46] However, the functional significance of sialylation on complement proteins remains poorly understood. Several works point to a role for glycosylation on complement proteins in controlling immune function. Gerard et al. showed that the de-N-glycosylated form of C5a desArg, a dearginated proinflammatory anaphylatoxin derived from C5a, was 10- to 12-fold more potent.[47] In contrast, Kontermann and Rauterberg showed that de-N-glycosylation of C9 dampened the cell lysis activity of C9.[48] Glycosylation can also play a role in controlling both serum half-life and resistance to proteolytic cleavage, which is of particular importance to this cascade.[9,38] The α2,6-sialylation may be increasing half-life, prolonging the cell-mediated damage from the cascade. There may also be other effects of α2,6-sialylation on complement biology that have yet to be discovered. In general, glycosylation as an aspect of complement has long been ignored. As we seek to develop therapeutic approaches to reverse the detrimental responses from the complement cascade observed in COVID-19, we will need to understand the functional impact of α2,6-sialylation and other glycans on complements.

METHODS

Cohorts and Sample Collection. COVID-19 plasma samples were collected from 71 patients recruited from the Intensive Care Unit, the hospital ward, or the outpatient clinic at the University Hospital (Edmonton, Alberta, Canada). The CoCollab study was reviewed and approved by the Research Ethics Board/Alberta Research Information Servies (ARISE) at the University of Alberta. Recruits were informed of the details of the study by the study team, had the opportunity to ask questions, and then signed informed consent. Plasma samples analyzed in this study were collected at the time of enrollment. Blood samples were processed within 1 h where possible to isolate plasma and peripheral blood mononuclear cells and then aliquoted into 100 μL cryovials.

Non-COVID-19 plasma samples were collected from 60 adults originally recruited for a study of influenza vaccination response among the general population, at the University of Georgia Clinical and Translational Research Unit (Athens, Georgia, U.S.A.) from September 2019 to December 2019. All volunteers were enrolled with written, informed consent.

https://doi.org/10.1021/acsinfecdis.2c00421
ACS Infect. Dis. XXXX, XXX, XXX−XXX

Participants were excluded if they, at the time of enrollment, already received the seasonal influenza vaccine, had acute or chronic conditions that would put the participant at risk for an adverse reaction to the blood draw or the flu vaccine (e.g., Guillain-Barré syndrome or allergies to egg products), or had conditions that could skew the analysis (e.g., recent flu symptoms or steroid injections/medications). Plasma samples analyzed in this present study were collected prior to vaccination. A brief description of the two cohorts is in Table S1.

Hospital-based autopsies for COVID-19 patients were performed at NYU Winthrop Hospital (Mineola, New York, U.S.A.) among persons with laboratory-confirmed COVID-19 or who were under investigation and tested positive on post-mortem PCR. Autopsies were performed between the dates of March 2020 and April 2020. The lungs, heart, kidneys, and liver were used in this study. Tissues were fixed in 10% buffered formalin for 72 h and routinely processed. Details about the clinical characteristics of the COVID-19 cohort and of the matched COVID-19-negative cohort can be found in Table S2.

Fluorescent Labeling of Samples. Total protein concentrations of plasma and autopsy samples were determined with DC protein assay (Bio-Rad Laboratories). PBS refers to phosphate-buffered saline (137 mM NaCl, 2.7 mM KCl, 8.9 mM Na_2HPO_4, and 1.8 mM KH_2PO_4, pH = 7.4) hereinafter. PBST refers to PBS supplemented with Tween 20 (concentration in v/v indicated where it appears) hereinafter.

To label plasma proteins, each sample containing 10 μg of total protein was first diluted in PBS to 27 μL. The pH of the solution was adjusted with 3 μL of 1 M sodium bicarbonate. Then 0.21 μL of a 10 mg/mL Alexa Fluor 555 NHS ester (Thermo Fisher Scientific) stock solution was thoroughly mixed with the sample solution. The mixture was incubated in the dark and at room temperature with gentle agitation. After 1 h, unconjugated dyes were removed by Zeba dye and biotin removal filter plates (Thermo Fisher Scientific). The reference standard, a commercial human plasma (MilliporeSigma, catalog no. P9523), was fluorescently labeled with Alexa Fluor 647 NHS ester (Thermo Fisher Scientific) in a similar fashion. The amounts of reagents were scaled linearly to the starting protein amount (2 mg). Finally, each Alexa Fluor 555-labeled sample (10 μg of total protein) was mixed with a proper volume of Alexa Fluor 647-labeled reference standard containing the same amount of protein. The dual-color mixture was first diluted to 50 μL with PBS and then mixed with 50 μL of 0.1% PBST.

To label tissue samples from autopsy, each sample containing 50 μg of total protein was first diluted in PBS to 60 μL. The pH of the solution was adjusted with 6.7 μL of 1 M sodium bicarbonate. Then 0.2 μL of a 10 mg/mL Alexa Fluor 555 NHS ester (Thermo Fisher Scientific) stock solution was thoroughly mixed with the sample solution. The mixture was incubated in the dark and at room temperature with gentle agitation. After 1 h, unconjugated dyes were removed by Zeba dye and biotin removal filter plates (Thermo Fisher Scientific). The pool reference was generated and fluorescently labeled with Alexa Fluor 647 NHS ester (Thermo Fisher Scientific) in a similar fashion. Then, each Alexa Fluor 555-labeled sample (3 μg of protein) was mixed with a proper volume of Alexa Fluor 647-labeled reference standard containing the same amount of protein. The dual-color mixture was first diluted to 74 μL with PBS and then mixed with 2 μL of 0.2% PBST.

Fabrication of Lectin Microarray Slides. Lectin microarray slides were fabricated as previously described.[13] In brief, lectins and antibodies were printed on Nexterion Slide H (Applied Microarrays) with the microarray printer NanoPlotter 2.1 (GeSim). The temperature and humidity inside the printer chamber were maintained at 14 °C and 50%, respectively. Inhibiting sugars were added to lectin solutions to a final concentration of 50 mM (except lactose, at 25 mM) prior to printing. Lectins for printing, concentrations, and inhibiting sugars are listed in Table S3 (for plasma samples) and Table S4 (for autopsy samples).

Dual-Color Lectin Microarray. All steps were performed in the dark at room temperature. Each dual-color mixture was allowed to hybridize with the microarrays for 1 h. Microarrays were washed twice with 0.005% PBST for 10 min and once with PBS for 5 min. The slides were briefly rinsed with ultrapure water and dried by centrifugation. Fluorescence signals were gained with Genepix 4400A fluorescence slide scanner (Molecular Devices) in the 532 and 635 nm channels, which correspond to the excitation/emission profiles of Alexa Fluor 555 and Alexa Fluor 647, respectively. Raw fluorescence signals and background signals were generated by the Genepix Pro 7 software (Molecular Devices) and were further processed and analyzed with a custom script as previously described.[27] Heatmaps, box plots, and volcano plots were generated with R (version 4.0.1). Annotation of lectin specificities was performed in accordance with the literature.[16]

Lectin Pulldown of Plasma Samples. In this section, centrifugation (1000 × *g*, 2 min) was used to remove liquid from the columns in washes and elutions. All steps were performed at room temperature. To prepare SNA-agarose columns, 200 μL of 50% suspension of streptavidin-agarose resin (MilliporeSigma) was added to each microcentrifuge column. The storage buffer was removed, and the resin was washed with 200 μL of PBS. Four hundred μL of biotinylated *Sambucus nigra* lectin (SNA, Vector Laboratories, prediluted to 0.5 mg/mL with PBS) was added to the column, and the mixture was incubated with gentle agitation for 30 min. Then the resin was washed with 200 μL of PBS twice. Control columns were prepared using the same procedure except that 400 μL of PBS was added to the column instead of biotinylated SNA.

To prepare SNA pulldown samples for mass spectrometry analysis, pooled plasma samples corresponding to the mild and severe COVID-19 patient groups were prepared by combining equal volumes of individual samples. Each pooled plasma sample containing 300 μg of total protein was diluted to 300 μL with PBS. Pulldown was performed in triplicate (i.e., each pooled sample was enriched with three separate columns prepared with the same procedure at the same time). Diluted samples were incubated with the SNA-bound resin or the control resin for 1 h with gentle agitation. The resin was washed with 400 μL of PBS three times. To elute glycoproteins, 75 μL of 0.2 M lactose in PBS was added to the column and incubated with gentle agitation. After 30 min, the flow-through was collected. Then 75 μL of 0.2 M lactose in 0.2 M acetic acid was added to the column and incubated with gentle agitation. After 30 min, the flow-through was collected and combined with the previous flow-through. Finally, the pH of the combined eluate was adjusted with 1 M Tris (pH = 9.0) to 7.5.

To prepare SNA pulldown samples for Western blotting, pooled plasma samples corresponding to the mild COVID-19,

https://doi.org/10.1021/acsinfecdis.2c00421
ACS Infect. Dis. XXXX, XXX, XXX−XXX

severe COVID-19, and negative control groups were prepared by combining equal volumes of individual samples. Albumin was depleted from each pooled sample with Pierce Albumin Depletion Kit (Thermo Fisher Scientific). Albumin-depleted sample protein concentrations were determined with DC protein assay (Bio-Rad Laboratories). Each albumin-depleted pooled plasma sample containing 200 μg of total protein was diluted to 300 μL with PBS. Diluted samples were incubated with the resin for 1 h with gentle agitation. The resin was washed with 400 μL of PBS three times. To elute glycoproteins, 75 μL of 0.2 M lactose in PBS was added to the column and incubated with gentle agitation. After 30 min, the flow-through was collected. Then 75 μL of 0.2 M lactose in 0.2 M acetic acid was added to the column and incubated with gentle agitation. After 30 min, the flow-through was collected and combined with the previous flow-through. The combined eluate was then dialyzed against PBS.

Mass Spectrometry and Protein Identification. Trypsin digestion was performed on the samples. Samples were reduced (200 mM DTT in 50 mM bicarbonate) and alkylated (200 mM iodoacetamide in 50 mM bicarbonate) before trypsin (6 ng/μL, Promega Sequencing grade) was added to a ratio of 1:20. The digestion was done overnight (~16 h) at 37 °C, and formic acid was then added to adjust the pH to 2−4. The samples were then dried, redissolved in 4% acetonitrile and 0.1% formic acid, and desalted using C18 tips (Thermo Scientific).

Peptides were resolved and ionized by using nano-flow high-performance liquid chromatography (HPLC) (Easy-nLC 1000, Thermo Scientific) coupled to a Q Exactive Orbitrap mass spectrometer (Thermo Scientific) with an EASY-Spray capillary HPLC column (ES800A, 75 μm × 15 cm, 100 Å, 3 μm, Thermo Scientific). The mass spectrometer was operated in data-dependent acquisition mode, recording high-accuracy and high-resolution survey orbitrap spectra using external mass calibration, with a resolution of 35 000 and m/z range of 300−1700. The 12 most intense multiply charged ions were sequentially fragmented by using HCD dissociation, and spectra of their fragments were recorded in the orbitrap at a resolution of 17 500; after fragmentation all precursors selected for dissociation were dynamically excluded for 30 s. Data was processed using Proteome Discoverer 1.4 (Thermo Scientific), and the database Uniprot Human UP000005640 was searched using SEQUEST (Thermo Scientific). Search parameters included a strict false discovery rate (FDR) of 0.01, a relaxed FDR of 0.05, a precursor mass tolerance of 10 ppm, and a fragment mass tolerance of 0.01 Da. Peptides were searched with carbamidomethyl cysteine as a static modification and oxidized methionine and deamidated glutamine and asparagine as dynamic modifications.

Protein quantitation was based on the number of peptide spectral matches (PSM). First, detected proteins (PSM ≥ 1 in at least one sample) were searched in the online portal of CRAPOme,[49] a database of protein contaminants in proteomic experiments. CRAPOme outputs a ratio of [num of expt (found/total)] for each query protein. Any protein with a [num of expt (found/total)] > 0.2 is considered a contaminant and removed.

To identify nonspecifically binding proteins, two-tailed Student's t test was performed between the PSM of the proteins in the triplicates of the pulldown samples and corresponding bead-only controls (PSM_{PD} and PSM_{CT}, respectively). Any protein that satisfies (1) average $PSM_{PD} \leq$ average PSM_{CT}, or (2) $PSM_{PD} < 2$, or (3) p-value of the t test >0.05 is removed. The remaining proteins are the SNA-enriched proteins and are listed in Table S5 (severe COVID-19) and Table S6 (mild COVID-19).

To identify significantly upregulated proteins in SNA-enriched severe COVID-19 plasma, two-tailed Student's t test was performed between the PSM of the enriched proteins in the triplicates of the severe sample and the mild sample (PSM_{severe} and PSM_{mild}, respectively). Any protein that satisfies (1) average PSM_{severe} > average PSM_{mild} and (2) p-value of the t test <0.05 is considered significantly upregulated in severe COVID-19 plasma and is listed in Table S7.

Western Blotting. All steps were conducted at room temperature unless noted otherwise. The column eluate, or the corresponding input (albumin-depleted plasma) containing 20 μg of total protein, was mixed with Laemmli buffer to a final volume of 200 μL. Then 100 μL of each sample was heated at 90 °C before being resolved by 4−20% sodium dodecyl sulfate−polyacrylamide gel electrophoresis (SDS-PAGE). Proteins were transferred to a nitrocellulose membrane, which was then stained with Ponceau S. After the total protein stain was erased, the membrane was blocked with a blocking buffer (PBS with 3% (w/v) bovine serum albumin (BSA) and 0.05% (v/v) Tween 20, pH = 7.4) for 1 h. Then the membrane was incubated with primary antibodies prediluted to 1 μg/mL in the blocking buffer for 1 h. Rabbit anti-human complement C5 antibody (clone no. EPR19699-24, Abcam, catalog no. ab202039) and mouse anti-human complement C9 antibody (clone no. X197, Hycult Biotech, catalog no. HM2111) were used for C5 and C9 detection, respectively. The membrane was washed with 0.05% PBST three times for 5 min per wash and then incubated with secondary antibodies prediluted to 0.1 μg/mL in the blocking buffer for 15 min. CF640-conjugated, goat anti-rabbit IgG antibody (MilliporeSigma, catalog no. SAB4600399) and IRDye 800CW-conjugated, goat anti-mouse IgG antibody (LI-COR, catalog no. 926-32210) were used for C5 and C9 primary antibody detection, respectively. Finally, the membrane was washed with 0.05% PBST three times for 5 min per wash before imaging.

Immunofluorescence Staining. Formalin-fixed, paraffin-embedded autopsy tissues was sectioned at 5 μm on Plus Slides (Fisher Scientific, catalog no. 22-042-924) and stored at room temperature prior to use. Sections were probed with the following reagents: Cy5 conjugated *Sambucus nigra* lectin (SNA, Vector Laboratories, catalog no. CL-1303); recombinant His-tagged divalent carbohydrate-binding Module 40[50] (diCBM40); recombinant His-tagged Griffithsin[51] (GRFT, plasmid gift from Dr. Weston Struwe, University of Oxford). Lectin fluorescent histochemistry, protein binding fluorescence, and chromogenic immunohistochemistry were performed on a Roche Ventana Discovery XT platform using Ventana reagents and detection kits unless otherwise noted. Sections were preincubated at 60 °C followed by online deparaffinization (Discovery Wash catalog no. 950-150). SNA (1.0 mg/mL), diCBM40 (0.8 mg/mL), and GRFT (1.0 mg/mL) were diluted 1:100 in Carbo-Free Blocking Solution (Vector Laboratories catalog no. SP-5040, lot no. ZG0630) and incubated for 3 h at room temperature. diCBM40 and GFRT were detected with Alexa Fluor 555 conjugated, mouse anti-6xHis Tag antibody (1.0 mg/mL, Thermo Fisher Scientific, catalog no. MA1-21315-A555, lot no. WD326765, RRID: AB_557403) diluted 1:100 in Carbo-Free Blocking Solution and incubated for 60 min. Labeled sections were

https://doi.org/10.1021/acsinfecdis.2c00421
ACS Infect. Dis. XXXX, XXX, XXX−XXX

washed in distilled water, counterstained with 100.0 ng/mL DAPI, and coverslipped with Prolong Gold antifade media.

Immunohistochemistry Staining. Single and multiplex-chromogenic immunohistochemistry were performed using unconjugated mouse anti-human interleukin-6 (clone no. OTI3G9, Origene, catalog no. TA500067, lot no. VE2990982), unconjugated murine anti-human Vimentin (clone no. V9, Ventana Medical Systems, catalog no. 790-2917, lot no. E04396, RRID:AB-2335925) and unconjugated mouse anti-human CD-163 clone MRQ-26 (Ventana Medical Systems catalog no. 760-4437, lot no. V001041, RRID: AB_2335969), unconjugated murine anti-human ST6 β-galactoside α2,6-sialyltransferase 1 (clone no. LN1, Thermo Fisher Scientific, catalog no. MA5-11900, lot no. XC3519066A, RRID: AB_10980157), unconjugated murine anti-human Pan-Cytokeratin (PanK, Thermo Fisher Scientific cat no. MA1-82041, lot no. 985542A RRID: AB_2335731), unconjugated mouse anti-human complement C9 antibody (clone no. X197, Hycult Biotech, catalog no. HM2111, lot no. 16152M0714-B, RRID: AB_2067596), and unconjugated mouse anti-human terminal complement complex C5b-9 (clone no. aEll, Dako Cytomation, catalog no. M0777, lot no. 20027911, RRID: AB_2067162). Antibodies were tested and sequence-optimized on a composite 30-core tissue microarray containing both normal and tumor tissues. All samples were sectioned at four microns and collected onto Plus microscope slides (Fisher Scientific, catalog no. 22-042-924) and stored at room temperature prior to use. Sections for IL-6 were preincubated at 60 °C followed by online deparaffinization (Discovery Wash, catalog no. 950-150). Anti-IL-6 was diluted 1:50 (20.0 μg/mL) in Ventana Antibody Diluent (catalog no. 760-219) and incubated for 5 h at room temperature. Primary antibody was detected using goat anti-mouse horseradish peroxidase conjugated multimer incubated for 8 min. The complex was visualized with 3,3-diaminobenzidine and enhanced with copper sulfate. Slides were washed in distilled water, counterstained with hematoxylin, dehydrated, and mounted with permanent media.

Multiplex samples were assayed with a tissue microarray for positive, negative, and multiplex crossover control. Multiplex-chromogenic immunohistochemistry was performed on a Ventana Medical Systems Discovery Ultra using Ventana reagents and detection kits unless otherwise specified. In brief, slides for sequential Vimentin-CD163 multiplex were heated at 60 °C for 1 h and deparaffinized on-instrument. Antigen retrieval was performed in CC1 (TRIS-Borate-EDTA, pH = 8.5, Roche, catalog no. 950-224) for 32 min at 95 °C followed by treatment with 3% hydrogen peroxide for 8 min to quench endogenous peroxidase. Anti-Vimentin was applied neat for 20 min at 37 °C followed by detection with goat anti-mouse horseradish peroxidase conjugated multimer and visualized with purple (TAMRA) chromogen. Slides were denatured in instrument wash buffer (Atlas Antibodies, catalog no. 950-330) at 95 °C for 32 min to strip immunological reagents followed by application of hydrogen peroxide for 8 min to quench horseradish peroxidase. Anti-CD163 was applied neat and incubated for 60 min at 37 °C followed by detection with goat anti-rabbit horseradish peroxidase conjugated multimer and visualized with yellow (DABsyl) chromogen. All slides were washed in distilled water, counterstained with hematoxylin, dehydrated, and mounted with permanent media.

Sections for C9 were antigen retrieved using Cell Conditioner 1 (Tris-Borate-EDTA, pH = 8.5, catalog no. 950-500) for 20 min and C5b9 treated with Protease-3 (catalog no. 760-2020) for 12 min. Anti-C9 (1.0 μg/mL) and C5b9 (0.045 mg/mL) antibody were diluted 1:100 in TBSA (25 mM Tris, 15 mM NaCl, 1% BSA, pH = 7.2) and incubated for 3 h at room temperature. Primary antibody was detected using goat anti-mouse horseradish peroxidase conjugated multimer incubated for 8 min. The complex was visualized with 3,3-diaminobenzidine and enhanced with copper sulfate. Slides were washed in distilled water, counterstained with hematoxylin, dehydrated, and mounted with permanent media. Negative controls were incubated with diluent only.

Chromogenic IHC and histochemistry were whole-slide scanned on a Leica Aperio AT2 at 40×. Samples were viewed using eSlideManager (version 12.3.2.5030) and bright-field images captured via Imagescope (version 12.3.3.5048).

Analysis of Whole-Blood RNA-seq Data Sets. Publicly available whole-blood RNA sequencing data and raw counts analyzed in this work were downloaded from Gene Expression Omnibus (GSE161731) published in a study by McClain et al.[32] and analyzed in GraphPad Prism.

Statistical Analysis. Unpaired, two-tailed Mann−Whitney U test and Student's t test were used for statistical analysis in this study. When statistical analysis is performed, the type of test used and p-value annotation are indicated in the corresponding figure captions or in the corresponding subsections of the Methods section. All statistics were done using the R software package (R version 4.1.0, https://www.r-project.org/).

■ ASSOCIATED CONTENT

Data Availability Statement

Lectin microarray data for plasma samples and autopsy samples are available at Synapse.org (DOI: 10.7303/syn27791795).

Supporting Information

The Supporting Information is available free of charge at https://pubs.acs.org/doi/10.1021/acsinfecdis.2c00421.

> Data visualization for lectin microarray data for plasma and autopsy samples from COVID-positive and -negative patients; histochemical analysis of lectin binding in COVID 19 autopsy livers; ST6GAL1 expression in COVID-positive lungs and livers; ST6GAL1 and C5 expression in whole blood; IL-6 and CD163 staining of autopsy samples; cohort characteristics; lectin microarray printlists; and mass spectrometry analysis (PDF)

■ AUTHOR INFORMATION

Corresponding Author

Lara K. Mahal − *Department of Chemistry, University of Alberta, Edmonton, Alberta T6G 2G2, Canada;* orcid.org/0000-0003-4791-8524; Email: lkmahal@ualberta.ca

Authors

Rui Qin − *Department of Chemistry, University of Alberta, Edmonton, Alberta T6G 2G2, Canada*

Emma Kurz − *Department of Cell Biology, NYU Grossman School of Medicine, New York, New York 10016, United States*

https://doi.org/10.1021/acsinfecdis.2c00421
ACS Infect. Dis. XXXX, XXX, XXX−XXX

Shuhui Chen − *Department of Chemistry, Biomedical Research Institute, New York University, New York, New York 10003, United States*
Briana Zeck − *Center for Biospecimen Research and Development, NYU Langone, New York, New York 10016, United States;* orcid.org/0000-0003-1864-4034
Luis Chiribogas − *Center for Biospecimen Research and Development, NYU Langone, New York, New York 10016, United States*
Dana Jackson − *University of Alberta Hospital, Edmonton, Alberta T6G 2B7, Canada*
Alex Herchen − *University of Alberta Hospital, Edmonton, Alberta T6G 2B7, Canada*
Tyson Attia − *University of Alberta Hospital, Edmonton, Alberta T6G 2B7, Canada*
Michael Carlock − *Center for Vaccines and Immunology, University of Georgia, Athens, Georgia 30605, United States*
Amy Rapkiewicz − *Department of Pathology, NYU Long Island School of Medicine, Mineola, New York 11501, United States*
Dafna Bar-Sagi − *Department of Biochemistry and Molecular Pharmacology, NYU Grossman School of Medicine, New York, New York 10016, United States*
Bruce Ritchie − *University of Alberta Hospital, Edmonton, Alberta T6G 2B7, Canada*
Ted M. Ross − *Center for Vaccines and Immunology, University of Georgia, Athens, Georgia 30605, United States*

Complete contact information is available at: https://pubs.acs.org/10.1021/acsinfecdis.2c00421

Author Contributions

◆Co-first authorship.

Author Contributions

L.K.M. designed the study; D.J., A.H., T.A., B.R., M.C., E.K., and A.R. collected the samples; R.Q., E.K., S.C., L.C., and B.Z. performed the experiments; R.Q., E.K., S.C., and L.K.M. analyzed the data; R.Q., E.K., S.C., and L.K.M. wrote the paper; D.B.-S., T.M.R., and L.K.M. supervised the study.

Notes

The authors declare no competing financial interest.

■ ACKNOWLEDGMENTS

The authors thank the Alberta Proteomics and Mass Spectrometry Facility for providing mass spectrometry services. The NYULH Center for Biospecimen Research and Development, Histology and Immunohistochemistry Laboratory (RRID:SCR_018304) is supported in part by the Laura and Isaac Perlmutter Cancer Center Support Grant (NIH/NCI P30CA016087). This project has been funded by the National Institute of Allergy and Infectious Diseases, a component of the NIH, Department of Health and Human Services, under Contract 75N93019C00052 (T.M.R and L.K.M.) and the Canada Excellence Research Chair Program (L.K.M.). Some graphical content was created with biorender.com.

■ REFERENCES

(1) Hu, B.; Guo, H.; Zhou, P.; Shi, Z. L. Characteristics of SARS-CoV-2 and COVID-19. *Nat. Rev. Microbiol* **2021**, *19*, 141−154.
(2) Kaur, S.; Tripathi, D. M.; Yadav, A. The Enigma of Endothelium in COVID-19. *Front Physiol* **2020**, *11*, 989.
(3) Gustine, J. N.; Jones, D. Immunopathology of Hyper-inflammation in COVID-19. *Am. J. Pathol.* **2021**, *191*, 4−17.
(4) Afzali, B.; Noris, M.; Lambrecht, B. N.; Kemper, C. The state of complement in COVID-19. *Nat. Rev. Immunol* **2022**, *22*, 77−84.
(5) Zuo, Y.; Yalavarthi, S.; Shi, H.; Gockman, K.; Zuo, M.; Madison, J. A.; Blair, C.; Weber, A.; Barnes, B. J.; Egeblad, M.; Woods, R. J.; Kanthi, Y.; Knight, J. S. Neutrophil extracellular traps (NETs) as markers of disease severity in COVID-19. *medRxiv* **2020**, DOI: 10.1101/2020.04.09.20059626.
(6) Risitano, A. M.; Mastellos, D. C.; Huber-Lang, M.; Yancopoulou, D.; Garlanda, C.; Ciceri, F.; Lambris, J. D. Complement as a target in COVID-19? *Nat. Rev. Immunol* **2020**, *20*, 343−344.
(7) Qin, R.; Mahal, L. K. The host glycomic response to pathogens. *Curr. Opin Struct Biol.* **2021**, *68*, 149−156.
(8) Irvine, E. B.; Alter, G. Understanding the role of antibody glycosylation through the lens of severe viral and bacterial diseases. *Glycobiology* **2020**, *30*, 241−253.
(9) Varki, A. Biological roles of glycans. *Glycobiology* **2017**, *27*, 3−49.
(10) Heindel, D. W.; Koppolu, S.; Zhang, Y.; Kasper, B.; Meche, L.; Vaiana, C. A.; Bissel, S. J.; Carter, C. E.; Kelvin, A. A.; Elaish, M.; Lopez-Orozco, J.; Zhang, B.; Zhou, B.; Chou, T. W.; Lashua, L.; Hobman, T. C.; Ross, T. M.; Ghedin, E.; Mahal, L. K. Glycomic analysis of host response reveals high mannose as a key mediator of influenza severity. *Proc. Natl. Acad. Sci. U. S. A.* **2020**, *117*, 26926−26935.
(11) Larsen, M. D.; de Graaf, E. L.; Sonneveld, M. E.; Plomp, H. R.; Nouta, J.; Hoepel, W.; Chen, H. J.; Linty, F.; Visser, R.; Brinkhaus, M.; Sustic, T.; de Taeye, S. W.; Bentlage, A. E. H.; Toivonen, S.; Koeleman, C. A. M.; Sainio, S.; Kootstra, N. A.; Brouwer, P. J. M.; Geyer, C. E.; Derksen, N. I. L.; Wolbink, G.; de Winther, M.; Sanders, R. W.; van Gils, M. J.; de Bruin, S.; Vlaar, A. P. J.; Amsterdam, U. C.; Rispens, T.; den Dunnen, J.; Zaaijer, H. L.; Wuhrer, M.; van der Schoot, C. E.; Vidarsson, G., et al. Afucosylated IgG characterizes enveloped viral responses and correlates with COVID-19 severity. *Science* **2021**, *371*; DOI: 10.1126/science.abc8378
(12) Chakraborty, S.; Gonzalez, J.; Edwards, K.; Mallajosyula, V.; Buzzanco, A. S.; Sherwood, R.; Buffone, C.; Kathale, N.; Providenza, S.; Xie, M. M.; Andrews, J. R.; Blish, C. A.; Singh, U.; Dugan, H.; Wilson, P. C.; Pham, T. D.; Boyd, S. D.; Nadeau, K. C.; Pinsky, B. A.; Zhang, S.; Memoli, M. J.; Taubenberger, J. K.; Morales, T.; Schapiro, J. M.; Tan, G. S.; Jagannathan, P.; Wang, T. T. Proinflammatory IgG Fc structures in patients with severe COVID-19. *Nat. Immunol* **2021**, *22*, 67−73.
(13) Pilobello, K. T.; Agrawal, P.; Rouse, R.; Mahal, L. K. Advances in lectin microarray technology: optimized protocols for piezoelectric print conditions. *Curr. Protoc Chem. Biol.* **2013**, *5*, 1−23.
(14) Pilobello, K. T.; Slawek, D. E.; Mahal, L. K. A ratiometric lectin microarray approach to analysis of the dynamic mammalian glycome. *Proc. Natl. Acad. Sci. U. S. A.* **2007**, *104*, 11534−11539.
(15) AHS. https://www.alberta.ca/stats/covid-19-alberta-statistics.htm#variants-of-concern (accessed Sep 23, 2022).
(16) Bojar, D.; Meche, L.; Meng, G.; Eng, W.; Smith, D. F.; Cummings, R. D.; Mahal, L. K. A Useful Guide to Lectin Binding: Machine-Learning Directed Annotation of 57 Unique Lectin Specificities. *ACS Chem. Biol.* **2022**, DOI: 10.1021/acschembio.1c00689.
(17) Kurz, E.; Chen, S.; Vucic, E.; Baptiste, G.; Loomis, C.; Agrawal, P.; Hajdu, C.; Bar-Sagi, D.; Mahal, L. K. Integrated Systems Analysis of the Murine and Human Pancreatic Cancer Glycomes Reveals a Tumor-Promoting Role for ST6GAL1. *Mol. Cell Proteomics* **2021**, *20*, 100160.
(18) Chen, S.; Kasper, B.; Zhang, B.; Lashua, L. P.; Ross, T. M.; Ghedin, E.; Mahal, L. K. Age-Dependent Glycomic Response to the 2009 Pandemic H1N1 Influenza Virus and Its Association with Disease Severity. *J. Proteome Res.* **2020**, *19*, 4486−4495.
(19) Heindel, D. W.; Chen, S.; Aziz, P. V.; Chung, J. Y.; Marth, J. D.; Mahal, L. K. Glycomic Analysis Reveals a Conserved Response to Bacterial Sepsis Induced by Different Bacterial Pathogens. *ACS Infect Dis* **2022**, *8*, 1075−1085.
(20) Qin, R.; Meng, G.; Pushalkar, S.; Carlock, M. A.; Ross, T. M.; Vogel, C.; Mahal, L. K. Prevaccination Glycan Markers of Response to

an Influenza Vaccine Implicate the Complement Pathway. *J. Proteome Res.* **2022**, *21*, 1974−1985.
(21) Legrand, M.; Bell, S.; Forni, L.; Joannidis, M.; Koyner, J. L.; Liu, K.; Cantaluppi, V. Pathophysiology of COVID-19-associated acute kidney injury. *Nat. Rev. Nephrol* **2021**, *17*, 751−764.
(22) Rapkiewicz, A. V.; Mai, X.; Carsons, S. E.; Pittaluga, S.; Kleiner, D. E.; Berger, J. S.; Thomas, S.; Adler, N. M.; Charytan, D. M.; Gasmi, B.; Hochman, J. S.; Reynolds, H. R. Megakaryocytes and platelet-fibrin thrombi characterize multi-organ thrombosis at autopsy in COVID-19: A case series. *EClinicalMedicine* **2020**, *24*, 100434.
(23) Agrawal, P.; Kurcon, T.; Pilobello, K. T.; Rakus, J. F.; Koppolu, S.; Liu, Z.; Batista, B. S.; Eng, W. S.; Hsu, K. L.; Liang, Y.; Mahal, L. K. Mapping posttranscriptional regulation of the human glycome uncovers microRNA defining the glycocode. *Proc. Natl. Acad. Sci. U. S. A.* **2014**, *111*, 4338−4343.
(24) Koo, H. J.; Lim, S.; Choe, J.; Choi, S. H.; Sung, H.; Do, K. H. Radiographic and CT Features of Viral Pneumonia. *Radiographics* **2018**, *38*, 719−739.
(25) Beltrame, M. H.; Catarino, S. J.; Goeldner, I.; Boldt, A. B. W.; de Messias-Reason, I. J. The lectin pathway of complement and rheumatic heart disease. *Front Pediatr.* **2015**, *2*, 148.
(26) Ozaki, M.; Kang, Y.; Tan, Y. S.; Pavlov, V. I.; Liu, B.; Boyle, D. C.; Kushak, R. I.; Skjoedt, M. O.; Grabowski, E. F.; Taira, Y.; Stahl, G. L. Human mannose-binding lectin inhibitor prevents Shiga toxin-induced renal injury. *Kidney Int.* **2016**, *90*, 774−782.
(27) Lo, M. W.; Kemper, C.; Woodruff, T. M. COVID-19: Complement, Coagulation, and Collateral Damage. *J. Immunol* **2020**, *205*, 1488−1495.
(28) Ma, L.; Sahu, S. K.; Cano, M.; Kuppuswamy, V.; Bajwa, J.; McPhatter, J.; Pine, A.; Meizlish, M.; Goshua, G.; Chang, C. H.; Zhang, H.; Price, C.; Bahel, P.; Rinder, H.; Lei, T.; Day, A.; Reynolds, D.; Wu, X.; Schriefer, R.; Rauseo, A. M.; Goss, C. W.; O'Halloran, J. A.; Presti, R. M.; Kim, A. H.; Gelman, A. E.; Cruz, C. D.; Lee, A. I.; Mudd, P.; Chun, H. J.; Atkinson, J. P.; Kulkarni, H. S. Increased complement activation is a distinctive feature of severe SARS-CoV-2 infection. *bioRxiv* **2021**, *6*, eabh2259.
(29) Lubbers, R.; van Essen, M. F.; van Kooten, C.; Trouw, L. A. Production of complement components by cells of the immune system. *Clin. Exp. Immunol.* **2017**, *188*, 183−194.
(30) Merle, N. S.; Church, S. E.; Fremeaux-Bacchi, V.; Roumenina, L. T. Complement System Part I - Molecular Mechanisms of Activation and Regulation. *Front Immunol* **2015**, *6*, 262.
(31) Kitagawa, H.; Paulson, J. C. Differential expression of five sialyltransferase genes in human tissues. *J. Biol. Chem.* **1994**, *269*, 17872−17878.
(32) McClain, M. T.; Constantine, F. J.; Henao, R.; Liu, Y.; Tsalik, E. L.; Burke, T. W.; Steinbrink, J. M.; Petzold, E.; Nicholson, B. P.; Rolfe, R.; Kraft, B. D.; Kelly, M. S.; Saban, D. R.; Yu, C.; Shen, X.; Ko, E. M.; Sempowski, G. D.; Denny, T. N.; Ginsburg, G. S.; Woods, C. W. Dysregulated transcriptional responses to SARS-CoV-2 in the periphery. *Nat. Commun.* **2021**, *12*, 1079.
(33) Katz, Y.; Revel, M.; Strunk, R. C. Interleukin 6 stimulates synthesis of complement proteins factor B and C3 in human skin fibroblasts. *Eur. J. Immunol.* **1989**, *19*, 983−988.
(34) Fang, C.; Zhang, X.; Miwa, T.; Song, W. C. Complement promotes the development of inflammatory T-helper 17 cells through synergistic interaction with Toll-like receptor signaling and interleukin-6 production. *Blood* **2009**, *114*, 1005−1015.
(35) Danobeitia, J. S.; Djamali, A.; Fernandez, L. A. The role of complement in the pathogenesis of renal ischemia-reperfusion injury and fibrosis. *Fibrogenesis Tissue Repair* **2014**, *7*, 16.
(36) Pandya, P. H.; Wilkes, D. S. Complement system in lung disease. *Am. J. Respir. Cell Mol. Biol.* **2014**, *51*, 467−473.
(37) Wendisch, D.; Dietrich, O.; Mari, T.; von Stillfried, S.; Ibarra, I. L.; Mittermaier, M.; Mache, C.; Chua, R. L.; Knoll, R.; Timm, S.; Brumhard, S.; Krammer, T.; Zauber, H.; Hiller, A. L.; Pascual-Reguant, A.; Mothes, R.; Bulow, R. D.; Schulze, J.; Leipold, A. M.; Djudjaj, S.; Erhard, F.; Geffers, R.; Pott, F.; Kazmierski, J.; Radke, J.; Pergantis, P.; Bassler, K.; Conrad, C.; Aschenbrenner, A. C.; Sawitzki, B.; Landthaler, M.; Wyler, E.; Horst, D.; Hippenstiel, S.; Hocke, A.; Heppner, F. L.; Uhrig, A.; Garcia, C.; Machleidt, F.; Herold, S.; Elezkurtaj, S.; Thibeault, C.; Witzenrath, M.; Cochain, C.; Suttorp, N.; Drosten, C.; Goffinet, C.; Kurth, F.; Schultze, J. L.; Radbruch, H.; Ochs, M.; Eils, R.; Muller-Redetzky, H.; Hauser, A. E.; Luecken, M. D.; Theis, F. J.; Conrad, C.; Wolff, T.; Boor, P.; Selbach, M.; Saliba, A. E.; Sander, L. E. SARS-CoV-2 infection triggers profibrotic macrophage responses and lung fibrosis. *Cell* **2021**, *184*, 6243−6261.
(38) Bas, M.; Terrier, A.; Jacque, E.; Dehenne, A.; Pochet-Beghin, V.; Beghin, C.; Dezetter, A. S.; Dupont, G.; Engrand, A.; Beaufils, B.; Mondon, P.; Fournier, N.; de Romeuf, C.; Jorieux, S.; Fontayne, A.; Mars, L. T.; Monnet, C. Fc Sialylation Prolongs Serum Half-Life of Therapeutic Antibodies. *J. Immunol* **2019**, *202*, 1582−1594.
(39) Morell, A. G.; Gregoriadis, G.; Scheinberg, I. H.; Hickman, J.; Ashwell, G. The role of sialic acid in determining the survival of glycoproteins in the circulation. *J. Biol. Chem.* **1971**, *246*, 1461−1467.
(40) Haseli, S.; Khalili, N.; Bakhshayeshkaram, M.; Sanei Taheri, M.; Moharramzad, Y. Lobar Distribution of COVID-19 Pneumonia Based on Chest Computed Tomography Findings; A Retrospective Study. *Arch. Acad. Emerg. Med.* **2020**, *8*, e55.
(41) Yuyun, X.; Lexi, Y.; Haochu, W.; Zhenyu, S.; Xiangyang, G. Early Warning Information for Severe and Critical Patients With COVID-19 Based on Quantitative CT Analysis of Lung Segments. *Front Public Health* **2021**, *9*, 596938.
(42) Margaroli, C.; Benson, P.; Sharma, N. S.; Madison, M. C.; Robison, S. W.; Arora, N.; Ton, K.; Liang, Y.; Zhang, L.; Patel, R. P.; Gaggar, A. Spatial mapping of SARS-CoV-2 and H1N1 lung injury identifies differential transcriptional signatures. *Cell Rep. Med.* **2021**, *2*, 100242.
(43) Wang, X.; Wen, Y.; Xie, X.; Liu, Y.; Tan, X.; Cai, Q.; Zhang, Y.; Cheng, L.; Xu, G.; Zhang, S.; Wang, H.; Wei, L.; Tang, X.; Qi, F.; Zhao, J.; Yuan, J.; Liu, L.; Zhu, P.; Ginhoux, F.; Zhang, S.; Cheng, T.; Zhang, Z. Dysregulated hematopoiesis in bone marrow marks severe COVID-19. *Cell Discovery* **2021**, *7*, 60.
(44) Shen, B.; Yi, X.; Sun, Y.; Bi, X.; Du, J.; Zhang, C.; Quan, S.; Zhang, F.; Sun, R.; Qian, L.; Ge, W.; Liu, W.; Liang, S.; Chen, H.; Zhang, Y.; Li, J.; Xu, J.; He, Z.; Chen, B.; Wang, J.; Yan, H.; Zheng, Y.; Wang, D.; Zhu, J.; Kong, Z.; Kang, Z.; Liang, X.; Ding, X.; Ruan, G.; Xiang, N.; Cai, X.; Gao, H.; Li, L.; Li, S.; Xiao, Q.; Lu, T.; Zhu, Y.; Liu, H.; Chen, H.; Guo, T. Proteomic and Metabolomic Characterization of COVID-19 Patient Sera. *Cell* **2020**, *182*, 59−72.
(45) Ritchie, G. E.; Moffatt, B. E.; Sim, R. B.; Morgan, B. P.; Dwek, R. A.; Rudd, P. M. Glycosylation and the complement system. *Chem. Rev.* **2002**, *102*, 305−320−319.
(46) Blaum, B. S.; Hannan, J. P.; Herbert, A. P.; Kavanagh, D.; Uhrin, D.; Stehle, T. Structural basis for sialic acid-mediated self-recognition by complement factor H. *Nat. Chem. Biol.* **2015**, *11*, 77−82.
(47) Gerard, C.; Hugli, T. E. Identification of classical anaphylatoxin as the des-Arg form of the C5a molecule: evidence of a modulator role for the oligosaccharide unit in human des-Arg74-C5a. *Proc. Natl. Acad. Sci. U. S. A.* **1981**, *78*, 1833−1837.
(48) Kontermann, R.; Rauterberg, E. W. N-deglycosylation of human complement component C9 reduces its hemolytic activity. *Mol. Immunol* **1989**, *26*, 1125−1132.
(49) Mellacheruvu, D.; Wright, Z.; Couzens, A. L.; Lambert, J. P.; St-Denis, N. A.; Li, T.; Miteva, Y. V.; Hauri, S.; Sardiu, M. E.; Low, T. Y.; Halim, V. A.; Bagshaw, R. D.; Hubner, N. C.; Al-Hakim, A.; Bouchard, A.; Faubert, D.; Fermin, D.; Dunham, W. H.; Goudreault, M.; Lin, Z. Y.; Badillo, B. G.; Pawson, T.; Durocher, D.; Coulombe, B.; Aebersold, R.; Superti-Furga, G.; Colinge, J.; Heck, A. J.; Choi, H.; Gstaiger, M.; Mohammed, S.; Cristea, I. M.; Bennett, K. L.; Washburn, M. P.; Raught, B.; Ewing, R. M.; Gingras, A. C.; Nesvizhskii, A. I. The CRAPome: a contaminant repository for affinity purification-mass spectrometry data. *Nat. Methods* **2013**, *10*, 730−736.
(50) Ribeiro, J. P.; Pau, W.; Pifferi, C.; Renaudet, O.; Varrot, A.; Mahal, L. K.; Imberty, A. Characterization of a high-affinity sialic acid-

https://doi.org/10.1021/acsinfecdis.2c00421
ACS Infect. Dis. XXXX, XXX, XXX−XXX

specific CBM40 from *Clostridium perfringens* and engineering of a divalent form. *Biochem. J.* **2016**, *473*, 2109−2118.
(51) Mori, T.; O'Keefe, B. R.; Sowder, R. C., 2nd; Bringans, S.; Gardella, R.; Berg, S.; Cochran, P.; Turpin, J. A.; Buckheit, R. W., Jr.; McMahon, J. B.; Boyd, M. R. Isolation and characterization of griffithsin, a novel HIV-inactivating protein, from the red alga Griffithsia sp. *J. Biol. Chem.* **2005**, *280*, 9345−9353.

https://doi.org/10.1021/acsinfecdis.2c00421
ACS Infect. Dis. XXXX, XXX, XXX−XXX